Article

Local probe of bulk and edge states in a fractional Chern insulator

https://doi.org/10.1038/s41586-024-08092-7

Received: 9 April 2024

Accepted: 20 September 2024

Published online: 20 November 2024

Check for updates

Zhurun Ji[1,2,3,9], Heonjoon Park[4,9], Mark E. Barber[1,2,3], Chaowei Hu[4], Kenji Watanabe[5,6], Takashi Taniguchi[5,6], Jiun-Haw Chu[4], Xiaodong Xu[4,7]✉ & Zhi-Xun Shen[1,2,3,8]✉

The fractional quantum Hall effect is a key example of topological quantum many-body phenomena, arising from the interplay between strong electron correlation, topological order and time-reversal symmetry breaking. Recently, a lattice analogue of the fractional quantum Hall effect at zero magnetic field has been observed, confirming the existence of a zero-field fractional Chern insulator (FCI). Despite this, the bulk–edge correspondence—a hallmark of a FCI featuring an insulating bulk with conductive edges—has not been directly observed. In fact, this correspondence has not been visualized in any system for fractional states owing to experimental challenges. Here we report the imaging of FCI edge states in twisted $MoTe_2$ (t-$MoTe_2$) using microwave impedance microscopy[1]. By tuning the carrier density, we observe the system evolving between metallic and FCI states, the latter of which exhibits insulating bulk and conductive edges, as expected from the bulk–boundary correspondence. Further analysis suggests the composite nature of the FCI edge states. We also observe the evolution of edge states across the topological phase transition as a function of interlayer electric field and reveal exciting prospects of neighbouring domains with different fractional orders. These findings pave the way for research into topologically protected one-dimensional interfaces between various anyonic states at zero magnetic field, such as gapped one-dimensional symmetry-protected phases with non-zero topological entanglement entropy, Halperin–Laughlin interfaces and the creation of non-abelian anyons.

Fractional quantum Hall (FQH) states are distinguished by an incompressible two-dimensional bulk with edge channels that conduct fractional charge[2–6]. Although charge sensing[7–9], shot noise[10,11] and scanning gate microscopy[12] measurements have provided promising evidence of fractionalization, direct visualization of FQH edge states and the enclosed bulk remains elusive. Imaging these one-dimensional chiral edge modes is crucial to understand their physical properties[13] and could also substantially enhance our ability to manipulate edge-state conduction for potential applications in anyonic braiding and topological quantum computing[14]. Previously, measurement of magneto-plasmon resonances provided information of the FQH edge states[15]. Recently, there has been imaging of in-gap unidirectional edge modes in synthetic quantum systems[16–19]. However, these bosonic systems lacked a fully insulating bulk, which prevented direct testing of the bulk–boundary correspondence in solids hosting FQH states.

Microwave impedance microscopy (MIM) is a powerful local probe of material conductivity[1] suitable for this purpose. MIM has been successfully used to image edge states in several topological systems, including quantum Hall[20,21] (among other methods[22,23]), quantum spin Hall insulator[24] and quantum anomalous Hall (QAH) insulators[25]. Despite this progress, imaging fractional edge states with MIM is challenging because of the stringent experimental requirements for forming FQH states, such as high magnetic field and sub-kelvin temperature.

The recent breakthrough in the realization of the fractional quantum anomalous Hall effect[26–30] provides a unique opportunity to image the fractional edge states. As well as the absence of magnetic field, the fractional quantum anomalous Hall effect can survive to above 1 K. For instance, nearly quantized Hall resistance (R_{xy}) with strongly suppressed longitudinal resistance (R_{xx}) are observed for the −2/3 FCI states at as high as 2 K in t-$MoTe_2$ bilayer[28]. These features make the zero-field FCI the ideal platform for visualizing fractional edge states.

The experimental realization of the fractional quantum anomalous Hall effect also accompanies several pressing questions. For instance, in transport studies, R_{xx} is suppressed but remains finite, which is probably from the disorder of the material platform, for example, moiré disorder[31]. Topological phase transitions have been inferred from transport measurements[28,29] but are not fully understood. Further, the formation and spatial characteristics of the fractional edge states require a local probe to explore. We address these questions by a scanning MIM probe with sub-100 nm spatial resolution.

[1]Department of Physics, Stanford University, Stanford, CA, USA. [2]Department of Applied Physics, Stanford University, Stanford, CA, USA. [3]Stanford Institute for Materials and Energy Sciences, SLAC National Accelerator Laboratory, Menlo Park, CA, USA. [4]Department of Physics, University of Washington, Seattle, WA, USA. [5]Research Center for Electronic and Optical Materials, National Institute for Materials Science, Tsukuba, Japan. [6]Research Center for Materials Nanoarchitectonics, National Institute for Materials Science, Tsukuba, Japan. [7]Department of Materials Science and Engineering, University of Washington, Seattle, WA, USA. [8]Geballe Laboratory for Advanced Materials, Stanford University, Stanford, CA, USA. [9]These authors contributed equally: Zhurun Ji, Heonjoon Park. ✉e-mail: xuxd@uw.edu; zxshen@stanford.edu

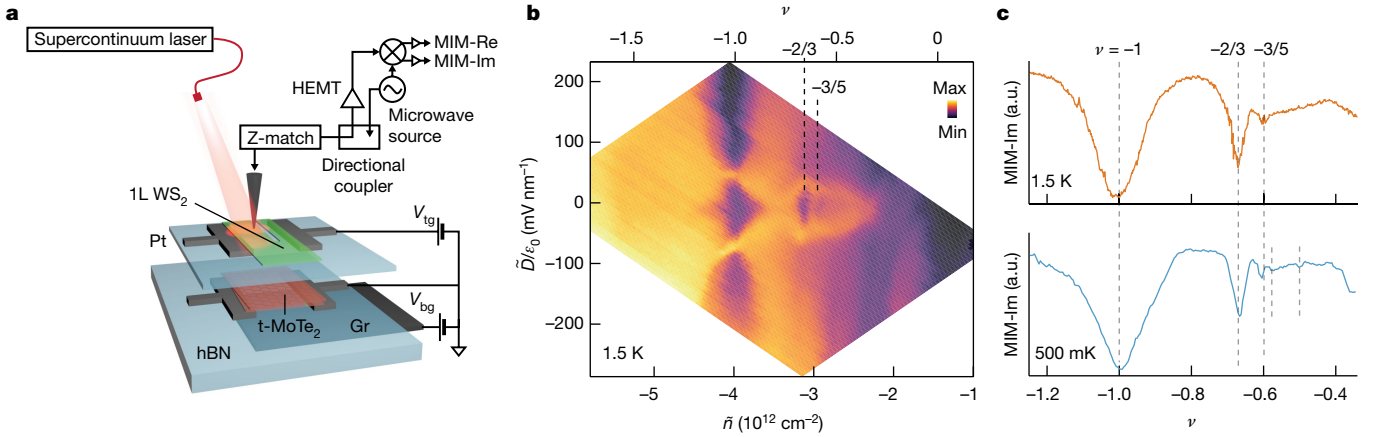

Fig. 1 | Local probe of bulk FCI states. a, Schematic of the ER-MIM setup and the t-$MoTe_2$ device. The dual-gated device has a monolayer (1L) WS_2 top gate (V_{tg}) and a graphite (Gr) bottom gate (V_{bg}). The sample is divided into dual-gated region 1 (left), region 2 (right) and a middle region, without a top gate. **b**, The MIM-Im signal as a function of displacement field ($\tilde{D}/\epsilon_0$) and carrier density ($\tilde{n}$) (calculated using geometric capacitance models, in region 1) at 1.5 K. The filling factor (ν) is shown on the top axis (see Methods). The location of this measurement is shown in Fig. 2a. **c**, MIM-Im signal versus filling factor ν at $T = 1.5$ K (top, orange curve), zero displacement field and $T = 500$ mK (bottom, blue curve). The suppression of the signal at several filling factors indicates the bulk insulating properties of Jain sequence FCI states. a.u., arbitrary units.

Experimental technique

We introduce the exciton-resonant MIM (ER-MIM) technique for sensing dual-gated t-$MoTe_2$ samples. A prevalent challenge with conventional MIM is the measurement of devices with a top gate, which typically screens the probe, thereby hindering the direct assessment of the underlying sample. We overcome this through both innovation in MIM technology and strategic sample design. The experimental configuration, depicted in Fig. 1a, comprises a microwave transmission line, impedance-matched to a metallic scanning probe (tip)[1,32–34], and optical access. The device consists of a t-$MoTe_2$ homobilayer with a 3.2° twist, encapsulated within hexagonal boron nitride (hBN) layers and graphite as a bottom gate. For the top gate, we chose a tungsten disulfide (WS_2) monolayer. Optical illumination of the entire sample near a photon energy resonant with the WS_2 A exciton (about 2.2 eV) induces the optical gating and photoconductive effect (details in ref. [35]), allowing the monolayer WS_2 to function as a tunable gate without screening microwaves from reaching the sample layer. As shown in Fig. 1a, a narrow channel was etched into the WS_2 layer using an atomic force microscopy (AFM) tip (see Methods), dividing the device into region 1 (left) and region 2 (right). All data are taken at zero magnetic field with a microwave frequency of 6.5 GHz. Our findings focus on MIM-Im, the imaginary component of the reflected microwave signal, which indicates the extent of microwave screening by the sample (or conductivity; also see Methods and Extended Data Fig. 2).

Local probe of bulk FCI states

The local probing capability of MIM allows us to explore the bulk properties of FCIs without edge effects, a challenging task for other methods. Figure 1b shows the MIM-Im intensity as a function of carrier density ($\tilde{n}$) and interlayer electric field ($\tilde{D}/\epsilon_0$) that serves to tune the layer polarization of the moiré orbitals. Here $\tilde{n}$ and $\tilde{D}$ are calculated using the geometric capacitance model (details in Methods). The data are taken at 1.5 K in region 1, indicated by the white star in Fig. 2a. The chosen colour scheme uses dark for insulating states and bright for conductive states, revealing a rich landscape of electronic phases. Near $\tilde{D}/\epsilon_0 = 0$, at which the system assumes a honeycomb lattice, there are three prominent doping regimes with insulating behaviour, centred at filling factors (ν) −1, −2/3 and −3/5. The system is conductive near −1/2 filling but becomes insulating at low doping levels, for example, near −1/3 filling (Extended Data Fig. 3). At large values of $|\tilde{D}/\epsilon_0|$, the charge carriers are fully polarized to a single layer forming a triangular lattice, and the system enters an insulating phase as seen from the dark line at commensurate fillings of $\nu = -1$ and dark regions near −2/3 and −1/2. At intermediate electric fields, a bright conductive region separates the insulating phases near zero and high $|\tilde{D}/\epsilon_0|$.

The MIM phase diagram of the bulk state presents a close resemblance to the Chern insulator phase diagram derived from longitudinal resistance (R_{xx}) measurements in transport studies. As detailed in ref. 28, a pronounced suppression of R_{xx} is observed in the QAH state near $\nu = -1$ and the FCI state near $\nu = -2/3$. This suppression is attributed to quantized edge-state transport, indicating insulating bulk states—a finding corroborated by our ER-MIM measurements. A finite but reduced R_{xx} near $\nu = -1/2$ aligns with the metallic response detected by means of MIM around this filling, which is linked to putative composite Fermi liquid states[36,37]. The application of a perpendicular electric field at $\nu = -1$, −2/3 and −1/2 induces a marked increase in R_{xx}, suggesting the emergence of either Mott or generalized Wigner crystal states[38–40] owing to full layer polarization. Our MIM measurement identifies an intermediate metallic phase among the electric-field-induced phase transition from Chern insulator to charge-ordered states, evidence of a closure of the electronic gap during this topological phase transition. Using the local probe of MIM, we can measure conductivity in pristine sample areas, circumventing moiré disorder and resolve more states. Figure 1c plots MIM-Im as a function of filling factor under zero displacement field at 1.5 K (orange) and 500 mK (blue). Distinct dips in conductivity are revealed at filling factors of −1, −2/3 and −3/5, indicating clearer FCI states compared with conventional transport measurements at the same temperature. Notably, at 500 mK, we observe a conductivity dip at −4/7 filling absent at 1.5 K, suggesting that its energy gap is smaller than the other two FCI states. Furthermore, a subtle but appreciable conductivity dip at $\nu = -1/2$ is observed at 500 mK. The weak dips near −4/7, −1/2 and other features at even lower fillings are dependent on position and only resolved in certain areas of the sample and remain a future direction to explore with cleaner devices.

Imaging QAH edge states

Scanning the metal tip enables us to explore the Chern insulator edge states. Figure 2a shows spatial maps of MIM-Im at selected filling factors, from −1.28 to −0.73. The white arrow in Fig. 2b indicates the parameter space for the panels in Fig. 2a, defined at a specific location in

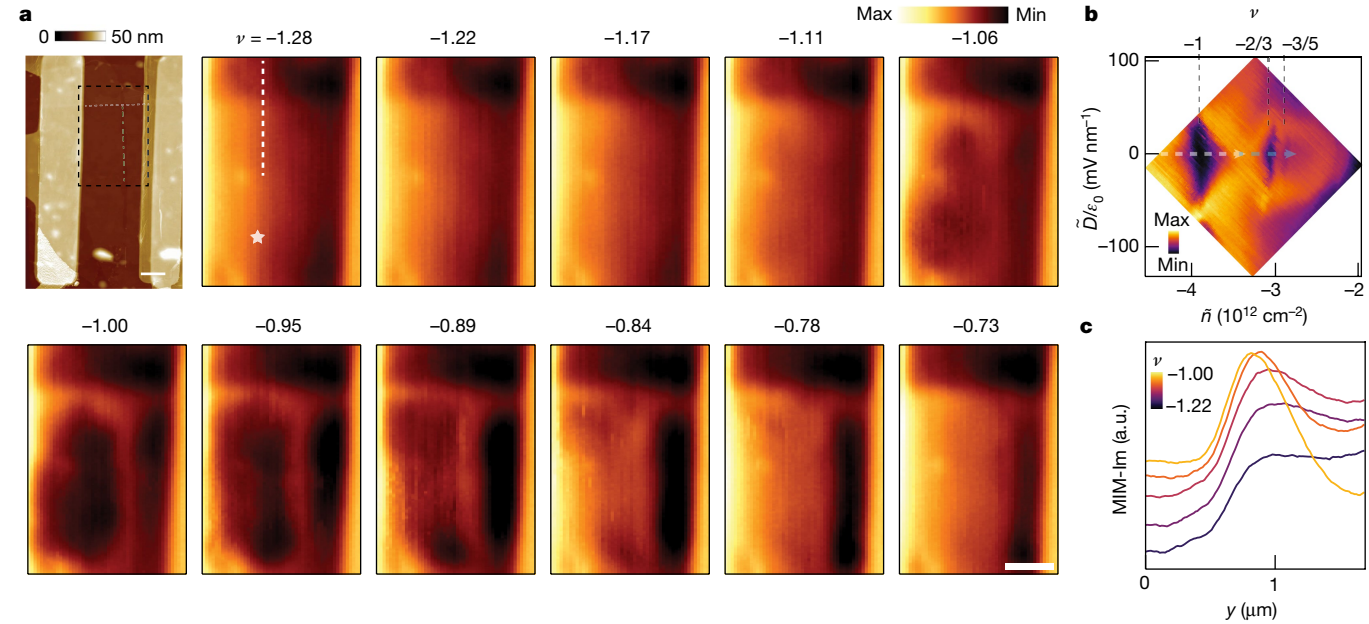

Fig. 2 | Imaging QAH edge states. a, First panel: AFM image of the sample, showing the edges and interfaces (grey and green dashed lines, respectively) and the scanning region (black rectangle). Scale bar, 1 μm. Other panels: real-space maps of the imaginary microwave response (MIM-Im) at different fillings, showing bulk–edge signal contrast being developed near filling $\nu = -1$. Scale bar, 1 μm. **b**, The MIM-Im signal as a function of displacement field ($\tilde{D}/\epsilon_0$) and carrier density ($\tilde{n}$) at 1.5 K, measured at the location denoted by the white star in **a**. The filling factor (ν) is shown on the top axis. The dashed white arrow denotes the electric field–carrier density conditions for obtaining the images in **a** and the dashed blue arrow denotes the electric field–carrier density conditions for obtaining the images in Fig. 3a. **c**, Linecuts averaged over 0.7 μm width around the dashed white line in **a** of MIM-Im signals (with vertical offsets) at different filling factors traversing the physical edge. a.u., arbitrary units.

region 1 (denoted by the white star in Fig. 2a). The first panel of Fig. 2a presents an AFM image of the sample, with the dashed black square highlighting the scan area. Below the dashed grey line lies the t-$MoTe_2$ region (Extended Data Fig. 1). Starting at $\nu = -1.28$, the entire sample area exhibits a large MIM-Im signal, indicating a metallic phase. As $|\nu|$ decreases, the bulk signal diminishes. At $\nu = -1$, the bulk is dark and the edges light up, consistent with a QAH state, that is, insulating in the bulk and conducting at the edge[25]. Further reducing the doping returns t-$MoTe_2$ to a metallic state. A similar behaviour can be seen in region 2. The bright stripe in the interface region is because of the absence of the top gate and hence a different carrier density.

We investigate the edge-state evolution versus doping by extracting the spatial dependence of MIM-Im amplitude at selected filling factors. The results, shown in Fig. 2c, are taken along the dashed line in the second panel of Fig. 2a. The spatial linecuts reveal two notable features. First, the width of the spatial profile narrows as ν approaches −1, indicative of the formation of QAH edge states. However, the full width at half maximum of about 500 nm is much larger than the tip spatial resolution (see Extended Data Fig. 2c for details). Second, the amplitude of the MIM-Im signal is higher in the QAH phase than in the metallic phase. Both phenomena can be attributed to the emergence of gapless collective edge magnetoplasmon (EMP) modes from the one-dimensional edge states circulating along the sample boundary, at which the width of the edge MIM peak corresponds to the characteristic EMP length scale, comparable with the sample diameter[41].

Imaging fractional edge states

Figure 3a shows MIM-Im spatial maps of the sample at carrier densities when the moiré Chern band is fractionally filled (along the dashed blue arrow in Fig. 2b). t-$MoTe_2$ becomes metallic when slightly under-doped from the QAH state, as shown by the strong MIM-Im signal over the entire sample area. Remarkably, as ν approaches the −2/3 filling, the map shows a dark bulk contrasted by bright edges, indicating that the corresponding −2/3 FCI state is insulating in the bulk and conductive at the edge. This pattern of edge conduction with an insulating bulk is also observed for the −3/5 FCI state. Figure 3b illustrates the evolution of the edge linecut signal as ν shifts from −0.71 (black curve) to the −2/3 FCI state (orange curve). Consistent with theoretical predictions[42,43], this trend closely mirrors that of the QAH state. As ν approaches the −2/3 filling, the bulk becomes insulating and the edge conduction becomes pronounced.

We also compare the edge-state signals between the FCI and QAH states. As depicted in Fig. 3c, the black, purple and orange curves represent the MIM-Im measurements at $\nu = -1$, −2/3 and −3/5 respectively, under the same conditions (see Extended Data Fig. 6 for spatial maps). The data reveal that the width of the FCI edge peak is similar to that of the QAH state, implying the formation of the EMP mode. Furthermore, the intensities differ.

The EMP resonance frequencies are determined by the edge velocity, localization length and Chern number[41]. At 6.5 GHz, the MIM-Im signal primarily reflects the first EMP resonance (details in Methods). Assuming a single-edge picture, this signal is affected by the following factors: the EMP resonance, which depends on σ_{xy}, shows that, for fractional states, the MIM-Im signal is expected to follow the order: MIM-Im$_{\nu=-1}$ < MIM-Im$_{\nu=-2/3}$ < MIM-Im$_{\nu=-3/5}$. Screening from σ_{xx}, reflecting the dielectric response of the sample, also follows this order. However, the experimental results show MIM-Im$_{\nu=-1}$ < MIM-Im$_{\nu=-2/3}$ ≈ MIM-Im$_{\nu=-3/5}$, suggesting contributions beyond these two factors. This implies the insufficiency of the single-edge picture or the composite nature of the fractional edge modes. Because our edge is a physical edge, there would be strong inter-channel interactions and scatterings present[44,45]. An applicable model would be the Kane, Fisher and Polchinski (KFP) picture[46]. Using the −2/3 state as an example, the KFP model describes the edge as consisting of a downstream charge channel (conductance (2/3) e^2/h) and an upstream neutral mode (zero net electric current). It explains the absence of incompressible stripe sensed by MIM at the

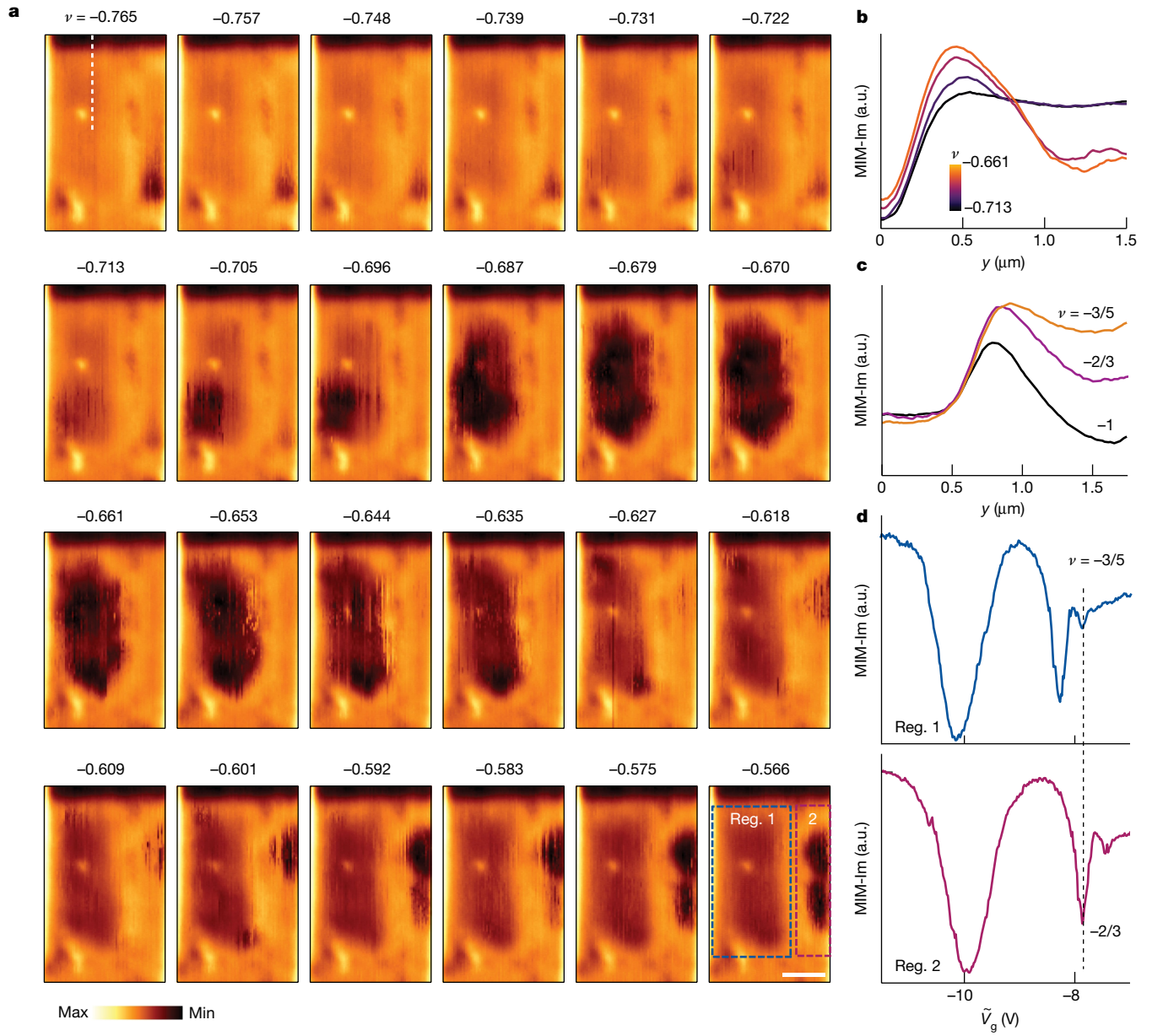

Fig. 3 | Imaging fractional edge states. a, Real-space maps of the imaginary microwave response at different fillings, showing bulk–edge signal contrast being developed near filling $\nu = -2/3$ and $\nu = -3/5$. Scale bar, 1 μm. **b**, Linecuts of MIM-Im signal averaged over 0.3 μm width around the dashed white line in **a** (in region 1), at a series of different filling factors between −0.661 and −0.713. **c**, Linecuts of MIM-Im signal traversing the edge at $\nu = -3/5$, −2/3 and −1, averaged over 0.5 μm width. Original data in Extended Data Fig. 5. **d**, MIM-Im signal versus $\tilde{V}_g = V_{bg} + C_{tg}/C_{bg}V_{tg}$ (where C_{tg} and C_{bg} are the geometric capacitance) at two representative locations in the two regions of the sample at $T = 1.5$ K, showing the coexistence of the two FCI states at $\nu = -3/5$ and $\nu = -2/3$. a.u., arbitrary units.

edge (with approximately 100 nm spatial resolution), but further details require exploration (see Methods).

The homogeneity of the device (Extended Data Fig. 5), combined with the larger thermodynamic gap of the fractional states in t-$MoTe_2$ (ref. 47), facilitates the imaging of bulk–edge correspondence. Besides, we observed adjacent domains of different FCI states. Figure 3d presents the MIM-Im signal versus gate voltage from two regions (dashed squares in Fig. 3a). Owing to the differences in gating efficiency in these two regions (Methods and Extended Data Figs. 1, 4 and 5), the −3/5 FCI state in regime 1 coexists with the −2/3 state in regime 2. The MIM signal in the interface region indicates a strongly scattered interface state. Future designs, such as split top gates, could enable independent control over these FCI states, facilitating the study of topologically protected one-dimensional interfaces formed between different anyonic orders[48] at zero magnetic field. These possibilities include the edge-state scattering/coupling between Halperin and Laughlin states, studying topological entanglement entropy of gapped one-dimensional states, creation of new anyonic states and future anyonic braiding operations[49].

Edge Evolution in Topological Transitions

Finally, we study the evolution of edge states during topological phase transitions induced by an out-of-plane electric field. Figure 4a shows the MIM-Im signal versus electric field of the $\nu = -3/5$ (red) and −2/3 (orange) FCI states and −1 (purple) QAH state. The MIM signal is suppressed at both low and high $|\bar{D}/\epsilon_0|$ but is pronounced in the intermediate regime. As previously discussed, this suggests a consecutive

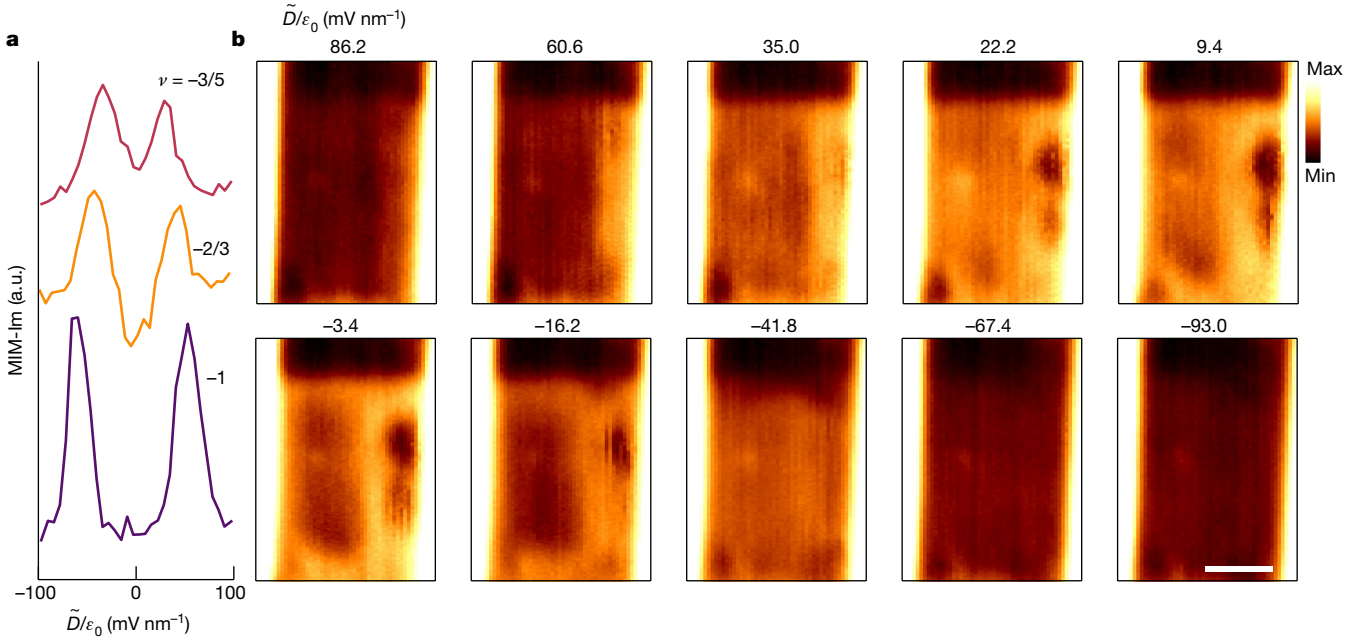

Fig. 4 | Edge-state evolution across electric-field-induced topological phase transition. a, MIM-Im signal as a function of $\tilde{D}/\epsilon_0$ at T = 1.5 K. Red, orange and purple curves plotted with vertical offsets correspond to the filling factors −3/5, −2/3 and −1 states, respectively. **b**, Real-space maps of MIM-Im at different displacement fields at ν = −2/3 filling factor, showing bulk–edge signal contrast being developed during the formation of the FCI state at small $|\tilde{D}/\epsilon_0|$. Scale bar, 1 µm. a.u., arbitrary units.

topological phase transition from the Chern insulator state to a metallic state and eventually to a correlated insulating state as $|D/\epsilon_0|$ increases from zero to a large value. Figure 4b depicts the MIM-Im image at selected electric fields for the −2/3 FCI state (Extended Data Fig. 7). At high electric fields, the system is in a correlated insulating state, resulting in a dim overall MIM-Im image. At the phase-transition boundary, the image brightens, reflecting the system entering a metallic state as the gap closes. Near $|\tilde{D}/\epsilon_0| = 0$, t-$MoTe_2$ is in the FCI state with a dark signal in the bulk and bright edges. The strong contrast of the edges at the FCI and the trivial insulating state confirms that the observed edge state for the FCI results from bulk–boundary correspondence and not trivial charge accumulation at the edges. Meanwhile, the distinction of non-trivial edges is evident for the −1 QAH state as expected (Extended Data Fig. 8). On the other hand, as shown in Extended Data Fig. 9, the −1/2 state at 1.5 K experiences a transition from a compressible state (or a weakly compressible state at certain spots) at small $|\tilde{D}/\epsilon_0|$ to an incompressible state at large $|\tilde{D}/\epsilon_0|$.

Summary

Using ER-MIM with a monolayer WS_2 top gate, we realize the first MIM measurements of dual-gated devices at zero magnetic field. This experimental breakthrough enables the visualization of both QAH and FCI states in t-$MoTe_2$, characterized by an insulating bulk and metallic edge, providing direct testing of the bulk–edge correspondence in the fractional quantum Hall effect. This conclusion is further substantiated by the distinction of scanning images across the topological phase transition tuned by electrical field. The comparative studies of the edge states between fractional and integer states, as well as among the various fractional states, suggest the composite nature of the FCI edge states. The results also reveal rich phenomena hidden in transport measurements owing to disorder, including nearby regions of distinct fractional orders and subtle fractional states. These observations suggest exciting future directions for the fractional quantum anomalous Hall effect with a highly controllable material platform.

Online content

Any methods, additional references, Nature Portfolio reporting summaries, source data, extended data, supplementary information, acknowledgements, peer review information; details of author contributions and competing interests; and statements of data and code availability are available at https://doi.org/10.1038/s41586-024-08092-7.

1. Barber, M. E., Ma, E. Y. & Shen, Z.-X. Microwave impedance microscopy and its application to quantum materials. *Nat. Rev. Phys.* **4**, 61–74 (2022).
2. Tsui, D. C., Stormer, H. L. & Gossard, A. C. Two-dimensional magnetotransport in the extreme quantum limit. *Phys. Rev. Lett.* **48**, 1559–1562 (1982).
3. Laughlin, R. B. Anomalous quantum Hall effect: an incompressible quantum fluid with fractionally charged excitations. *Phys. Rev. Lett.* **50**, 1395 (1983).
4. Halperin, B. I. Statistics of quasiparticles and the hierarchy of fractional quantized Hall states. *Phys. Rev. Lett.* **52**, 1583 (1984).
5. Arovas, D., Schrieffer, J. R. & Wilczek, F. Fractional statistics and the quantum Hall effect. *Phys. Rev. Lett.* **53**, 722 (1984).
6. Stern, A. Anyons and the quantum Hall effect—a pedagogical review. *Ann. Phys.* **323**, 204–249 (2008).
7. Goldman, V. & Su, B. Resonant tunneling in the quantum Hall regime: measurement of fractional charge. *Science* **267**, 1010–1012 (1995).
8. Martin, J. et al. Localization of fractionally charged quasi-particles. *Science* **305**, 980–983 (2004).
9. Radu, I. P. et al. Quasi-particle properties from tunneling in the ν = 5/2 fractional quantum Hall state. *Science* **320**, 899–902 (2008).
10. De-Picciotto, R. et al. Direct observation of a fractional charge. *Physica B* **249**, 395–400 (1998).
11. Bartolomei, H. et al. Fractional statistics in anyon collisions. *Science* **368**, 173–177 (2020).
12. Pascher, N. et al. Imaging the conductance of integer and fractional quantum Hall edge states. *Phys. Rev. X* **4**, 011014 (2014).
13. Chang, A. Chiral Luttinger liquids at the fractional quantum Hall edge. *Rev. Mod. Phys.* **75**, 1449 (2003).
14. Nayak, C., Simon, S. H., Stern, A., Freedman, M. & Sarma, S. D. Non-Abelian anyons and topological quantum computation. *Rev. Mod. Phys.* **80**, 1083 (2008).
15. Ashoori, R., Stormer, H., Pfeiffer, L., Baldwin, K. & West, K. Edge magnetoplasmons in the time domain. *Phys. Rev. B* **45**, 3894 (1992).
16. Stuhl, B., Lu, H.-I., Aycock, L., Genkina, D. & Spielman, I. Visualizing edge states with an atomic Bose gas in the quantum Hall regime. *Science* **349**, 1514–1518 (2015).
17. Yao, R. et al. Observation of chiral edge transport in a rapidly rotating quantum gas. *Nature* https://doi.org/10.1038/s41567-024-02617-7 (2024).
18. Mancini, M. et al. Observation of chiral edge states with neutral fermions in synthetic Hall ribbons. *Science* **349**, 1510–1513 (2015).
19. Wang, Z., Chong, Y., Joannopoulos, J. D. & Soljačić, M. Observation of unidirectional backscattering-immune topological electromagnetic states. *Nature* **461**, 772–775 (2009).

20. Lai, K. et al. Imaging of Coulomb-driven quantum Hall edge states. *Phys. Rev. Lett.* **107**, 176809 (2011).
21. Cui, Y.-T. et al. Unconventional correlation between quantum Hall transport quantization and bulk state filling in gated graphene devices. *Phys. Rev. Lett.* **117**, 186601 (2016).
22. Yacoby, A., Hess, H., Fulton, T., Pfeiffer, L. & West, K. Electrical imaging of the quantum Hall state. *Solid State Commun.* **111**, 1–13 (1999).
23. Suddards, M., Baumgartner, A., Henini, M. & Mellor, C. J. Scanning capacitance imaging of compressible and incompressible quantum Hall effect edge strips. *New J. Phys.* **14**, 083015 (2012).
24. Shi, Y. et al. Imaging quantum spin Hall edges in monolayer WTe_2. *Sci. Adv.* **5**, eaat8799 (2019).
25. Allen, M. et al. Visualization of an axion insulating state at the transition between 2 chiral quantum anomalous Hall states. *Proc. Natl Acad. Sci.* **116**, 14511–14515 (2019).
26. Cai, J. et al. Signatures of fractional quantum anomalous Hall states in twisted $MoTe_2$. *Nature* **622**, 63–68 (2023).
27. Zeng, Y. et al. Thermodynamic evidence of fractional Chern insulator in moiré $MoTe_2$. *Nature* **622**, 69–73 (2023).
28. Park, H. et al. Observation of fractionally quantized anomalous Hall effect. *Nature* **622**, 74–79 (2023).
29. Xu, F. et al. Observation of integer and fractional quantum anomalous Hall effects in twisted bilayer $MoTe_2$. *Phys. Rev. X* **13**, 031037 (2023).
30. Lu, Z. et al. Fractional quantum anomalous Hall effect in multilayer graphene. *Nature* **626**, 759–764 (2024).
31. Uri, A. et al. Mapping the twist-angle disorder and Landau levels in magic-angle graphene. *Nature* **581**, 47–52 (2020).
32. Chu, Z. et al. Unveiling defect-mediated carrier dynamics in monolayer semiconductors by spatiotemporal microwave imaging. *Proc. Natl Acad. Sci.* **117**, 13908–13913 (2020).
33. Cui, Y.-T., Ma, E. Y. & Shen, Z.-X. Quartz tuning fork based microwave impedance microscopy. *Rev. Sci. Instrum.* **87**, 063711 (2016).
34. Huang, X. et al. Correlated insulating states at fractional fillings of the WS_2/WSe_2 moiré lattice. *Nat. Phys.* **17**, 715–719 (2021).
35. Ji, Z. et al. Harnessing excitons at the nanoscale–photoelectrical platform for quantitative sensing and imaging. Preprint at https://arxiv.org/abs/2311.04211 (2023).
36. Dong, J., Wang, J., Ledwith, P. J., Vishwanath, A. & Parker, D. E. Composite Fermi liquid at zero magnetic field in twisted $MoTe_2$. *Phys. Rev. Lett.* **131**, 136502 (2023).
37. Goldman, H., Reddy, A. P., Paul, N. & Fu, L. Zero-field composite Fermi liquid in twisted semiconductor bilayers. *Phys. Rev. Lett.* **131**, 136501 (2023).
38. Regan, E. C. et al. Mott and generalized Wigner crystal states in WSe_2/WS_2 moiré superlattices. *Nature* **579**, 359–363 (2020).
39. Tang, Y. et al. Simulation of Hubbard model physics in WSe_2/WS_2 moiré superlattices. *Nature* **579**, 353–358 (2020).
40. Li, H. et al. Imaging two-dimensional generalized Wigner crystals. *Nature* **597**, 650–654 (2021).
41. Wang, T. et al. Probing the edge states of Chern insulators using microwave impedance microscopy. *Phys. Rev. B* **108**, 235432 (2023).
42. Lee, D.-H., Wang, Z. & Kivelson, S. Quantum percolation and plateau transitions in the quantum Hall effect. *Phys. Rev. Lett.* **70**, 4130 (1993).
43. Wen, X.-G. Theory of the edge states in fractional quantum Hall effects. *Int. J. Mod. Phys. B* **6**, 1711–1762 (1992).
44. Zülicke, U., MacDonald, A. & Johnson, M. Observability of counterpropagating modes at fractional quantum Hall edges. *Phys. Rev. B* **58**, 13778 (1998).
45. Sabo, R. et al. Edge reconstruction in fractional quantum Hall states. *Nat. Phys.* **13**, 491–496 (2017).
46. Kane, C., Fisher, M. P. & Polchinski, J. Randomness at the edge: theory of quantum Hall transport at filling ν=2/3. *Phys. Rev. Lett.* **72**, 4129 (1994).
47. Redekop, E. et al. Direct magnetic imaging of fractional Chern insulators in twisted $MoTe_2$ with a superconducting sensor. Preprint at https://arxiv.org/abs/2405.10269 (2024).
48. Dutta, B. et al. Distinguishing between non-abelian topological orders in a quantum Hall system. *Science* **375**, 193–197 (2022).
49. Nakamura, J., Liang, S., Gardner, G. C. & Manfra, M. J. Direct observation of anyonic braiding statistics. *Nat. Phys.* **16**, 931–936 (2020).

Methods

Sample fabrication

Single crystals of 2H-$MoTe_2$ were grown by Te self-flux. H_2 annealed Mo powder and Te lumps were first mixed at molar ratio near 1:200 and sealed in a quartz tube in vacuum. The tube was then placed in a muffle box furnace, which was heated up to 750 °C and slowly cooled to 500 °C at a rate of 1 K per hour. Finally, the crystals were separated from the flux and annealed in vacuum at 500 °C for a day to further remove the residual Te flux.

Full details of the sample fabrication procedure can be found in Extended Data Fig. 1. hBN and graphite flakes were exfoliated on Si/SiO_2 substrates and characterized using contrast-enhanced optical microscopy and AFM. First, the bottom gate structure was fabricated using a standard poly-(bisphenol A) carbonate-based dry transfer process. A hBN bottom gate dielectric was picked up, successively followed by a graphite bottom gate electrode and melted down on an intrinsic silicon substrate. The polycarbonate was washed off using chloroform and dichloromethane. The bottom gate was prepatterned using standard electron-beam lithography and Ti/Pt (2/5 nm) electrodes and Cr/Au (5/60 nm) conductive pads were deposited with electron-beam evaporation. Next, a monolayer $MoTe_2$ flake was exfoliated onto a silicon substrate inside a glovebox with O_2 and H_2O levels less than 0.1 ppm. The monolayer flake was cut in half using an AFM tip before the transfer to minimize strain. The t-$MoTe_2$ heterostructure was created by picking up part of the monolayer with a hBN top gate dielectric, rotating the transfer stage by a desired angle and picking up the remaining flake, before melting down onto the prepatterned bottom gate. Subsequently, further lithography and metal evaporation (Ti/Pt and Cr/Au) was performed to create electrodes and pads for the top gate. Finally, a monolayer WS_2 top gate was picked up and melted down on the stack to complete the dual-gated heterostructure. Contact-mode AFM was used to clean the surface between every step of the process to ensure the absence of polymer residue and bubbles. During the final step of cleaning, the AFM tip created a narrow channel within the monolayer WS_2 top gate that allows the formation of different Chern insulator domains.

Estimation of filling factor based on doping density

The carrier density $\tilde{n}$ and electric field $\tilde{D}$ on the sample were calculated from the top gate voltage V_{tg} and bottom gate voltage V_{bg} using the equations $\tilde{n} = (V_{tg}C_{tg} + V_{bg}C_{bg})/e - \tilde{n}_{offset}$ and $\tilde{D}/\epsilon_0 = (V_{tg}C_{tg} - V_{bg}C_{bg})/2\epsilon_0 - \tilde{D}_{offset}/\epsilon_0$, in which e is the electron charge, ϵ_0 is the vacuum permittivity and C_{tg} and C_{bg} are the top and bottom gate geometric capacitances, respectively. The capacitances were determined from the gate thickness measured by AFM. $\tilde{D}_{offset}$ was inferred from the dual-gate map at the probe location. The sequence of fractional fillings with prominent features in the dual-gate MIM-Im map (Fig. 1b) was used to identify the moiré filling factor.

MIM measurements

MIM measurements were performed in a 3-He cryostat with a 12 T superconducting magnet and homebuilt scanning setup. The MIM probe, an etched tungsten wire, was attached to a quartz tuning fork for topographic sensing and scans were taken with the tip held approximately 40 nm above the surface of the sample. MIM measures changes in admittance between the tip and the sample at GHz frequencies, which can be related to changes in local conductivity and permittivity in the sample (see Extended Data Fig. 2b for details). The input power is about 0.2 μW. The measurements reported here were carried out at 6.5 GHz at zero magnetic field. The optical coupling for ER-MIM was realized with a supercontinuum laser (NKT Photonics, FIU-20) that is fibre-coupled into a helium-3 cryostat. The wavelength was selected with a monochromator (Princeton Instruments, Acton SP2300), with a linewidth of around 0.5 nm. The laser power at the end of the 100-μm-diameter multimode fibre was approximately 0.1–1.0 mW throughout the measurements, with the spot radius at the end of the tip being around 0.8 mm. Extended Data Figs. 3–5 were taken in the second cooldown of the device, whereas all other data presented were taken in the first cooldown.

Finite-element simulation of the MIM response

Finite-element analysis of the MIM response to two-dimensional sheet conductance is shown in Extended Data Fig. 2. The tip radius is chosen to be 50 nm and the SiO_2 layer thickness 300 nm with $\kappa_{SiO2} = 3.9$. The MIM-Im response curve as a function of the sheet conductance of $\sigma_{t\text{-}MoTe2}$ is simulated. Simulations both with and without the gates were conducted and they differ by a scaling factor, so the simulation result is shown in arbitrary units.

A highly conductive state maximizes microwave screening, resulting in the largest MIM-Im signal in this reflection geometry, whereas an insulating state minimizes screening. In the case of our device, the WS_2 top gate layer partially screens microwave, which affects the MIM-Im signal contrast. Nonetheless, changes in the MIM-Im signal correlate with conductivity (screening capability) variations in the t-$MoTe_2$.

Within a more accurate theoretical framework[41], the MIM signal generation process is shown in Extended Data Fig. 2c. The tip has a time-varying carrier density owing to the externally applied microwave field, which generates an electrical potential at the sample. This electrical potential δV_s, gives rise to a sample carrier density change δn_s, with the carrier response function χ. δn_s in turn generates a δV_t at the tip. The MIM signal measures the tip–sample admittance Y, which captures this process of long-range Coulomb interaction between the tip and the sample and provides a measure of χ. When tip momentum $q \to 0$, the physical quantity being measured is the compressibility $\partial n/\partial \mu$.

Analysis of the EMP modes measured by MIM

Edge width. Following the discussion in ref. [41], in analysing the formation of EMPs, we consider the quantization of momentum $k = 2\pi n/P$, with n being an integer, owing to the finite sample perimeter P (or edge length). Our MIM operating frequency 6.5 GHz is well below the first EMP resonance, $\omega_{EMP}(2\pi/P)$, as the sample size is extremely small.

Consequently, the dominant contribution to the MIM response comes from the first EMP resonance frequency $\omega_{EMP}(k\omega)$, with magnitude determined by $1/(\omega - \omega_{EMP})$. The tip–sample admittance MIM measures $V_{t\text{-}s} \approx \log^2 k_{\omega 1} r \approx -\log^2 2\pi r/P$. Therefore, it predicts that, if at different fractional fillings the only difference among their EMP modes is the propagation velocity, while the width of MIM-Im decay from the edge would be similar. The line profiles of MIM-Im at different fractional fillings can be considered to have the functional form $b\log^2(ar) + c$ (in which a, b and c are parameters) and $1/a$ characterizes the edge width (although, to be more accurate, a convolution of tip resolution should be added; however, because the curves are measured under similar conditions, this does not change the qualitative result). Figure 3c shows that, for all three integer/fractional states, $\nu = -1$, $-2/3$ and $-3/5$, the edge width is similar.

Edge signal amplitude. The EMP resonance frequency is given by:

$$\hbar\omega_{EMP} = \hbar v q + \frac{Ce^2}{(2\pi)^2\epsilon_0} q \log\left(\frac{1}{ql}\right) \quad (1)$$

in which v is the edge velocity, l is the localization length, C is the Chern number of the Chern band and q is the one-dimensional momentum along the edge. The MIM-Im signal, as determined by $\mathrm{Im}Y_{ts}$, reads:

$$\mathrm{Im}Y_{ts} \approx \frac{k_\omega}{2\pi} \frac{\hbar\omega - \hbar\omega_{EMP}(k_\omega)}{(\hbar\omega - \hbar\omega_{EMP}(k_\omega))^2 + \epsilon^2} \quad (2)$$

in which ω is the excitation frequency, $\omega_{EMP}(k_\omega)$ is the resonance frequency and $\epsilon \approx \sigma_{xx}$ characterizes the dissipation[41].

EMP resonance related to σ_{xy}. Because the MIM frequency we are using ω = 6.5 GHz and the sample size is on the micrometre scale, ω is well below the first EMP resonance. In this limit of $\omega \ll \omega_{EMP}(2\pi/P)$, the bulk dissipation term ϵ does not greatly affect the signal. The edge signal is mainly determined by $1/\omega_{EMP}$. Comparing the ω_{EMP} of $\nu = -1$, $-2/3$ and $-3/5$ states and assuming that the quasiparticle charge of the fractional states follows the conductivity σ_{xy} measurement, the expected order is $\omega_{EMP,\nu=-3/5} < \omega_{EMP,\nu=-2/3} < \omega_{EMP,\nu=-1}$. Consequently, the MIM-Im signal would follow MIM-Im$_{\nu=-1}$ < MIM-Im$_{\nu=-2/3}$ < MIM-Im$_{\nu=-3/5}$.

Screening from non-vanishing σ_{xx}. Beyond EMP resonances, the MIM-Im signal measured at the edge reflects the screening capability of the sample (dielectric response), influenced by thermal excitation and density fluctuation. This is consistent with the bulk MIM-Im signal, favouring MIM-Im$_{\nu=-1}$ < MIM-Im$_{\nu=-2/3}$ < MIM-Im$_{\nu=-3/5}$.

Interaction and scattering between edges. Both the EMP resonance and dielectric screening predict MIM-Im$_{\nu=-1}$ < MIM-Im$_{\nu=-2/3}$ < MIM-Im$_{\nu=-3/5}$. However, the experimental result shows MIM-Im$_{\nu=-1}$ < MIM-Im$_{\nu=-2/3}$ ≈ MIM-Im$_{\nu=-3/5}$. This discrepancy implies that the model of a single-edge EMP mode for each fractional state is insufficient. However, if the downstream $2e^2/3h$ edge is formed by renormalization of downstream e^2/h and upstream $e^2/3h$ channels, as predicted by the KFP model, the EMP response, and hence MIM-Im signal, would deviate from that calculated for a single-mode EMP mode. The data hence provide insights into the composite nature of the edge modes. The prediction of the KFP model having only one charge channel also aligns with our findings that no extra edge mode or incompressible stripe[20] is detected beyond the tip resolution of approximately 100 nm. For future experiments, a gate-defined edge can be measured to explore the edge reconstruction in the limit of a smoothly varying confining potential[43,50]. This could help address questions on the fine edge-state structures[51–54].

Data availability

The data shown in the main figures are available in the Dryad data repository (https://doi.org/10.5061/dryad.9p8cz8ws0)[55]. Other data that support the findings of this study are available from the corresponding authors on reasonable request.

50. Meir, Y. Composite edge states in the *ν*=2/3 fractional quantum Hall regime. *Phys. Rev. Lett.* **72**, 2624 (1994).
51. Nakamura, J., Liang, S., Gardner, G. C. & Manfra, M. J. Fabry-Pérot interferometry at the *ν* = 2/5 fractional quantum Hall state. *Phys. Rev. X* **13**, 041012 (2023).
52. Santos, L. H., Cano, J., Mulligan, M. & Hughes, T. L. Symmetry-protected topological interfaces and entanglement sequences. *Phys. Rev. B* **98**, 075131 (2018).
53. Crépel, V., Claussen, N., Estienne, B. & Regnault, N. Model states for a class of chiral topological order interfaces. *Nat. Commun.* **10**, 1861 (2019).
54. Crépel, V., Claussen, N., Regnault, N. & Estienne, B. Microscopic study of the Halperin–Laughlin interface through matrix product states. *Nat. Commun.* **10**, 1860 (2019).
55. Ji, Z. et al. Original data for "Local probe of bulk and edge states in a fractional Chern insulator". *Dryad* https://doi.org/10.5061/dryad.9p8cz8ws0 (2024).

Acknowledgements We thank D. Lee, S. Kivelson and T. Wang for the stimulating discussions. This work at the Stanford Institute for Materials and Energy Sciences (SIMES) is supported by Quantum Sensing and Quantum Materials (QSQM), an Energy Frontier Research Center funded by the US Department of Energy (DOE), Office of Science, Basic Energy Sciences (BES), under award DE-SC0021238; as well as DOE grant through SIMES by the Department of Energy (DOE), Office of Science, Office of Basic Energy Sciences, Division of Materials Sciences and Engineering, under contract no. DE-AC02-76SF00515. Previous development of the MIM technique at Stanford University was funded in part by the Gordon and Betty Moore Foundation's EPiQS Initiative through grant GBMF4546 to Z.-X.S. Z.J. acknowledges support from the Stanford Science fellowship and the Urbanek-Chodorow Fellowship, as well as the Panofsky Fellowship of the SLAC National Accelerator Laboratory. The work at the University of Washington is mainly supported by DOE BES under award DE-SC0018171. Bulk $MoTe_2$ crystal growth is supported by the Center on Programmable Quantum Materials, an Energy Frontier Research Center funded by DOE BES under award DE-SC0019443. Device fabrication used the facilities and instrumentation supported by NSF MRSEC DMR-230879. K.W. and T.T. acknowledge support from the Elemental Strategy Initiative conducted by the MEXT, Japan (grant no. JPMXP0112101001) and JSPS KAKENHI (grant nos. 19H05790, 20H00354 and 21H05233).

Author contributions Z.-X.S. and X.X. initiated the collaboration. Z.J., H.P., X.X. and Z.-X.S. conceived the design of the experiment. Z.J. and M.E.B. carried out the ER-MIM measurements. H.P. fabricated the device. C.H. and J.-H.C. synthesized the bulk $MoTe_2$ crystals. K.W. and T.T. provided bulk hBN crystals. Z.J., H.P., X.X. and Z.-X.S. wrote the manuscript, with input from all authors.

Competing interests Z.-X.S. is a co-founder of PrimeNano Inc., which licensed the MIM technology from Stanford University. The other authors declare no competing interests.

Additional information

Supplementary information The online version contains supplementary material available at https://doi.org/10.1038/s41586-024-08092-7.

Correspondence and requests for materials should be addressed to Xiaodong Xu or Zhi-Xun Shen.

Peer review information *Nature* thanks Yonglong Xie and the other, anonymous, reviewer(s) for their contribution to the peer review of this work. Peer reviewer reports are available.

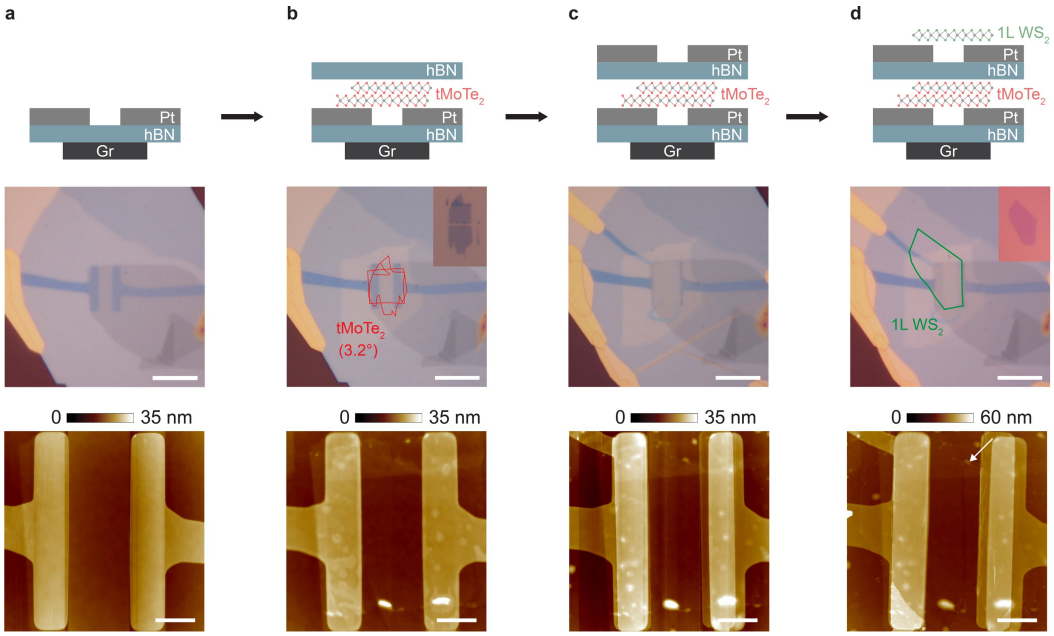

Extended Data Fig. 1 | Device-fabrication procedure. Each row indicates the device schematic, optical image and AFM image starting from the top. **a**, hBN/graphite bottom gate with prepatterned platinum (Pt) electrodes. **b**, A hBN/t-$MoTe_2$ stack is laid down on the bottom gate. Inset, optical image of 1L $MoTe_2$ flake that is cut in half using an AFM tip. **c**, Pt electrodes are patterned on top. **d**, A 1L WS_2 flake is laid down to serve as a top gate. Inset, optical image of 1L WS_2 flake. The white arrow indicates the tear within the 1L WS_2 top gate that defines domain 1 (left) and domain 2 (right). The interface region is only back-gated (when fringe field is not considered), whereas regions 1 and 2 are dual-gated. Scale bars in the optical images and AFM images are 10 μm and 2 μm, respectively.

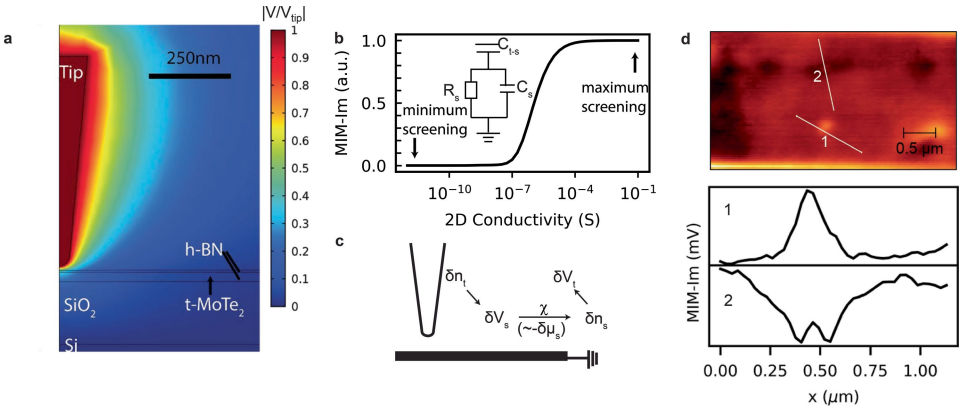

Extended Data Fig. 2 | MIM measurement details. a, Tip and sample device geometry and finite-element calculations of the quasi-static potential distribution (V). The colour plot is $|V/V_{tip}|$, with $\sigma = 10^{-12}$ S sq. **b**, Finite-element simulation result of the MIM-Im response curve as a function of the two-dimensional conductivity of the t-$MoTe_2$ sample. The inset diagram illustrates the lumped element model used to describe the system, in which $C_{t\text{-}s}$ represents the tip–sample coupling capacitance and R_s and C_s are the resistor and capacitor used to model the sample. Qualitatively, the MIM-Im signal indicates the extent of microwave screening by the sample. A highly conductive sample maximizes microwave screening, resulting in the largest MIM-Im signal in this reflection geometry, whereas an insulating sample minimizes screening. In this context, without loss of generality, we have chosen to focus solely on the MIM-Im channel because the MIM-Re response curve has a substantially poorer signal-to-noise ratio in our measurements[1]. **c**, Schematic showing the physical origin of the MIM signal[41]. The tip has a time-varying carrier density resulting from the externally applied microwave field, which generates an electrical potential at the sample. This electrical potential δV_s, gives rise to a sample carrier density change δn_s, with the carrier response function χ. δn_s, in turn, generates a δV_t at the tip. The MIM signal comes from the admittance Y measured at the tip, which captures this process of long-range Coulomb interaction between the tip and the sample and provides a measure of χ. When tip momentum $q \to 0$ or the tip–sample distance is large, the physical quantity being measured is $\partial n/\partial \mu$. **d**, Top, MIM-Im image measured at $V_{bg} = -7$ V and $V_{tg} = -2.35$ V. The tip–sample distance is around 40 nm. Bottom, two MIM-Im line profiles showing that the measurement can resolve features with a full width at half maximum of approximately 100 nm.

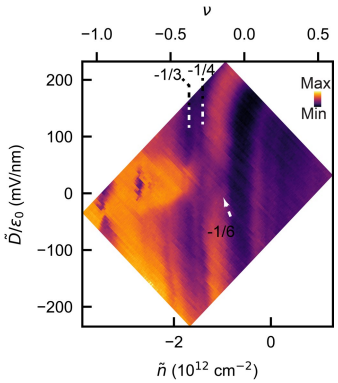

Extended Data Fig. 3 | The local probe of correlated insulating states in the lower filling regime. MIM-Im signal versus $\tilde{n}$ and $\tilde{D}/\epsilon_0$ in region 1 of the sample at $T = 1.5$ K, showing a series of correlated insulating states at low fillings.

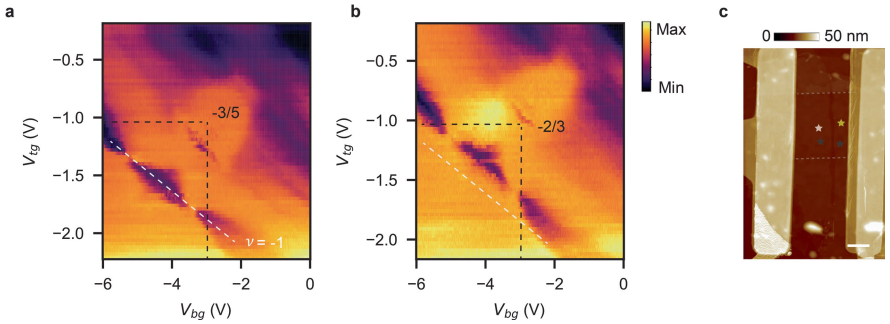

Extended Data Fig. 4 | Local probe of bulk FCI states in two regions of the sample. a,**b**, The MIM-Im signal as a function of back gate voltage (V_{bg}) and top gate voltage (V_{tg}) at 1.5 K in region 1 (**a**) and region 2 (**b**). The lines drawn in **a** and **b** are at the same locations. The white lines denote the $\nu = -1$ line for region 1. The black lines indicate the $\nu = -2/3$ and $\tilde{D} = 0$ voltage combinations in region 2, which, as shown in **a**, correspond to the $\nu = -3/5$ filling in region 1. **c**, The AFM image of the sample, showing the edges of the sample. Scale bar, 1 µm. The location of data taken for **a** and **b** are marked as a white star and a yellow star, respectively. The location of data taken for Fig. 3d representative of the two regions are marked as two black stars.

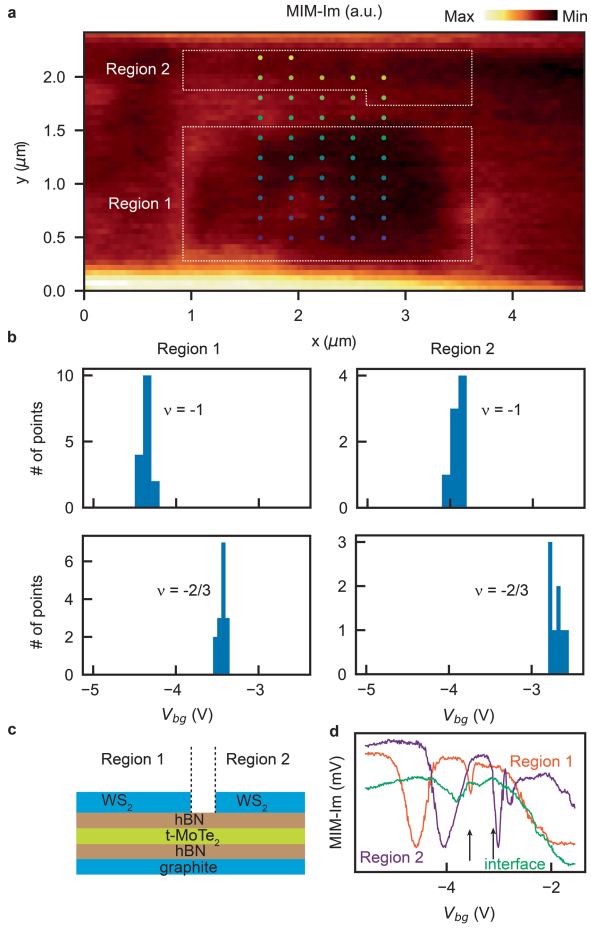

Extended Data Fig. 5 | Spatial homogeneity and details of the two regions (in the second cooldown of the device). a, The MIM-Im spatial map taken with $V_{tg} = -1.582$ V and $V_{bg} = -4.25$ V. The circles with different colours represent locations at which spectra discussed in **b** were taken. The two dashed white boxes denote the two regions. In this second cooldown, the homogeneity of the exposed top gate layer has deteriorated and hence the relationships of the filling factor and dual-gate voltage in the two regions (gating efficiencies) have discrepancies from the first cooldown. **b**, Histograms showing the distribution of V_{bg} of $\nu = -1$ and $\nu = -2/3$ dips in the two regions. **c**, Schematic of the cross-section of the device. The interface region is only back-gated, so it is compressible when region 1 and region 2 approach $\nu \approx -1$ (as shown in the phase diagram in Fig. 1b). **d**, Three representative MIM-Im plots measured at region 1, region 2 and the interface. The black arrows denote V_{bg} values at which the MIM-Im signal at the interface is affected by the formation of incompressible topological states with different fillings in regions 1 and 2. The MIM-Im signal enhancement indicates the formation of a strongly scattered interface state, coexisting with the metallic state.

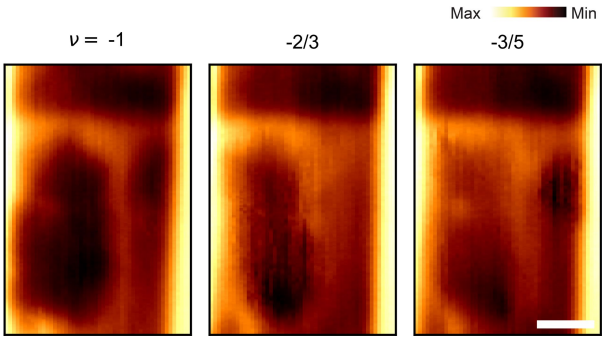

Extended Data Fig. 6 | Real-space maps of MIM-Im response for edge signal comparison. Real-space maps of the MIM-Im response at different fillings measured at $\nu = -1, -2/3$ and $-3/5$ for edge signal comparison. Scale bar, 1 µm.

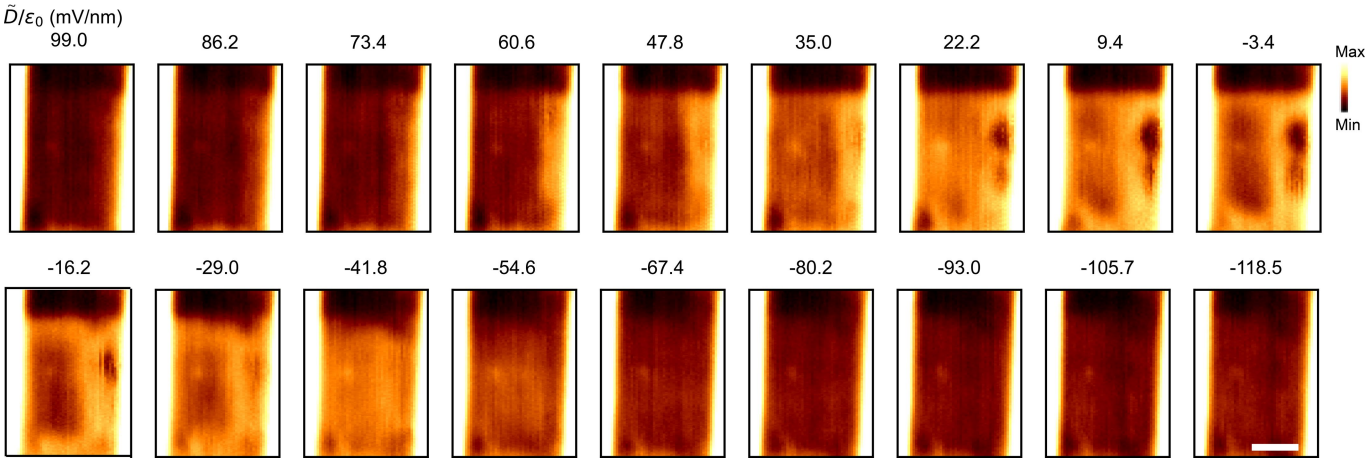

Extended Data Fig. 7 | Real-space maps of MIM-Im response at different displacement fields at $\nu = -2/3$ filling. Real-space maps of the MIM-Im at different displacement fields at $\nu = -2/3$ filling factor, showing the topological phase transition measured at $T = 1.5$ K. Scale bar, 1 µm.

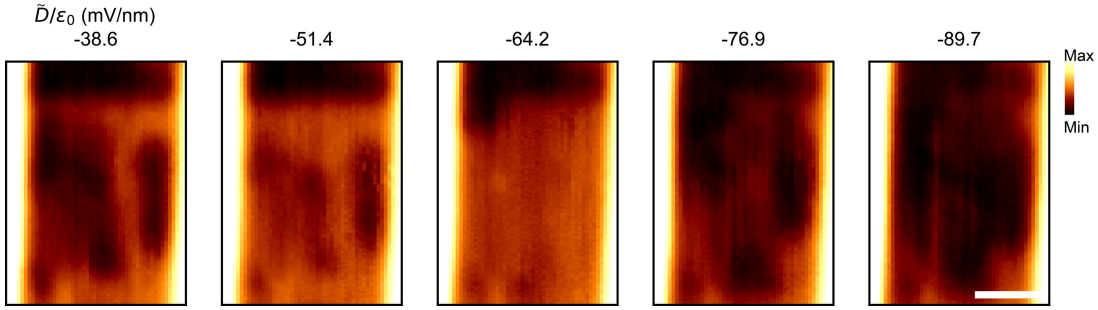

Extended Data Fig. 8 | Real-space maps of MIM-Im response at different displacement fields at $\nu = -1$ filling. Real-space maps of the MIM-Im at different displacement fields at $\nu = -1$ filling factor, presenting the transition from QAH state at small displacement field, to metallic, then to trivial insulating state at larger displacement fields measured at $T = 1.5$ K. The phase coexistence at the phase boundary is observed as the spatially inhomogeneous MIM-Im signal at certain displacement fields. Scale bar, 1 µm.

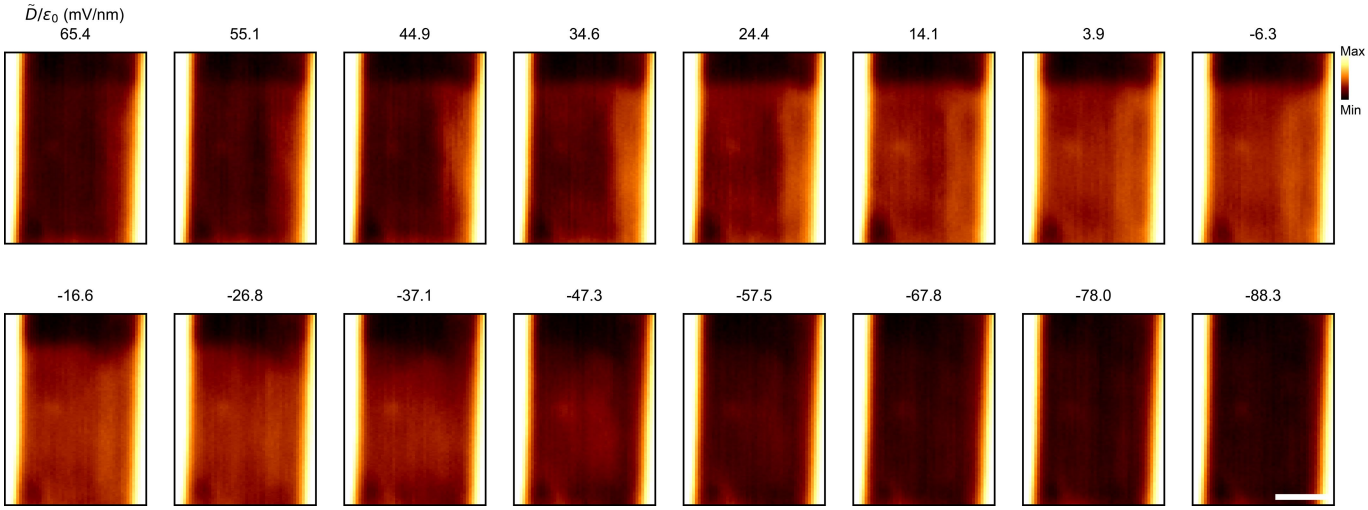

Extended Data Fig. 9 | Real-space maps of MIM-Im response at different displacement fields at $\nu = -1/2$ filling. Real-space maps of the MIM-Im at different displacement fields at $\nu = -1/2$ filling factor measured at $T = 1.5$ K. Scale bar, 1 µm.